

# Nature of Possible Magnetic Phases in Frustrated Hyperkagome Iridate

Ryuichi Shindou<sup>1,2,\*</sup>

<sup>1</sup>*International Center for Quantum Materials, Peking University, Beijing, China*

<sup>2</sup>*Collaborative Innovation Center of Quantum Matter, Beijing, China*

Based on Kitaev-Heisenberg model with Dzyaloshinskii-Moriya (DM) interactions, we studied nature of possible magnetic phases in frustrated hyperkagome iridate,  $\text{Na}_4\text{Ir}_3\text{O}_8$  (Na-438). Using Monte-Carlo simulation, we showed that the phase diagram is mostly covered by two competing magnetic ordered phases;  $Z_2$  symmetry breaking (SB) phase and  $Z_6$  SB phase, latter of which is stabilized by the classical order by disorder. These two phases are intervened by a first order phase transition line with  $Z_8$ -like symmetry. The critical nature at the  $Z_6$  SB ordering temperature is characterized by the 3D XY universality class, below which U(1) to  $Z_6$  crossover phenomena appears; the  $Z_6$  spin anisotropy becomes irrelevant in a length scale shorter than a crossover length  $\Lambda_*$  while becomes relevant otherwise. A possible phenomenology of polycrystalline Na-438 is discussed based on this crossover phenomena.

PACS numbers:

## I. INTRODUCTION

An interplay between spin and orbital degree of freedom enriches the physics of Mott insulators<sup>1</sup>. A strong relativistic spin-orbit interaction in cubic  $\text{IrO}_6$  octahedra endows Ir electron with spin-orbit entangled Kramers doublet (pseudo-spin doublet),<sup>2</sup> which opens a new root to “ $J = \frac{1}{2}$ ” Mott insulators with coordinate-dependent pseudo-spin-anisotropic exchange interactions.<sup>3–5</sup> Mott insulating materials with bond-dependent spin-anisotropic interactions possibly stabilize gapless quantum spin liquid state with exotic excitations such as Majorana fermions<sup>6</sup>. Honeycomb-lattice  $\text{Na}_2\text{IrO}_3$ ,<sup>7–10</sup>  $\alpha$ ,  $\beta$ ,  $\gamma$ - $\text{Li}_2\text{IrO}_3$ ,<sup>11,13,15</sup> and hyperkagome-lattice  $\text{Na}_4\text{Ir}_3\text{O}_8$  (Na-438)<sup>17–20</sup> are being intensively explored along this research interest. Throughout thermodynamic measurements,<sup>7,11,13,15</sup> resonant inelastic X-ray<sup>8,14,16</sup> and neutron scattering experiments<sup>9,10</sup>, the nature of low-temperature magnetic phases in all the honeycomb iridate compounds has been mostly clarified. Meanwhile nature of a low- $T$  phase of Na-438 is still veiled in mystery, although possible magnetic,<sup>5,26</sup> nematic<sup>21,24</sup>, valence bond solid,<sup>25</sup> and spin liquid phases<sup>22,23</sup> are being proposed theoretically. Early thermodynamic measurements such as magnetic specific heat, heat capacity, and magnetic susceptibility indicate spin liquid feature in Na-438<sup>17,18</sup>, while recent neutron scattering and muon spin relaxation experiments on powder samples suggest possibilities of a short-range ordered quasistatic spin state (dubbed as “configurationally degenerate phases with fluctuating order”) or spin-freezing like phase in Na-438<sup>19,20</sup>. One of the major obstacles toward comprehensive understanding of low- $T$  magnetic properties of Na-438 stems from its low crystal symmetry, which results in complexity of electronic band structure and effective exchange model of localized spins.<sup>5,27,28</sup>

In this paper, we introduce an effective spin exchange model for the hyperkagome iridate to obtain a comprehensive understanding of classical magnetism possible in Na-438. Based on a lattice parameter of Na-438, we

postulate additional lattice symmetries other than an exact crystal symmetry, to derive a relatively simpler but realistic effective spin model (Sec. II). Using Monte Carlo (MC) simulation and Luttinger-Tisza (LT) analysis, we derive a classical magnetic phase diagram for Na-438 (Sec. III). The phase diagram is mostly covered by two phases; one is  $Z_2$  symmetry breaking (SB) magnetic phase and the other is  $Z_6$  SB magnetic phase. The  $Z_6$  anisotropy in the latter phase is attributed to the entropy effect (Sec. IV). At finite temperature, these two phases are separated by a first order phase transition line with  $Z_8$  symmetry. The finite size scaling (FNS) analysis concludes that criticality at the ordering temperatures of  $Z_2$  and  $Z_6$  phases are characterized by the 3D Ising, and 3D XY universality class respectively. For a finite-size system, an intermediate temperature regime appears below the ordering temperature of  $Z_6$  phases, where the  $Z_6$  spin anisotropy becomes effectively irrelevant and spin ordering develops in a U(1) symmetric way. This crossover temperature regime  $\Delta T_* \equiv T_c - T_*$  is scaled with the linear dimension of the system size  $\Lambda$  as  $\Delta T_* \simeq \Lambda^{-\frac{1}{\nu_6}}$  with  $\nu_6 = 1.45 \sim 1.85$  (Sec. V). Effects of the quantum fluctuation are also mentioned in Sec. VI. A possible phenomenology of low- $T$  magnetic behaviors of the powder samples as well as a brief summary are given in Sec. VII.

## II. AN EXCHANGE SPIN MODEL FOR HYPERKAGOME IRIDATE

The hyperkagome lattice is a three-dimensional lattice which comprises of corner-sharing triangles (Fig. 1). The cubic unit cell contains 12 crystallographically distinct lattice points. Each sublattice point has a two-fold rotational axis, around which the lattice is symmetric under the  $C_2$  rotation;  $C_{2@j}$  ( $j = 1, 2, \dots, 12$ ) and  $j$  sublattice index. We can choose  $C_{2@j}$  ( $j = 1, \dots, 6$ ) as generators of the exact crystal symmetry group; the others six are identical to one of the generators ( $C_{2@7} = C_{2@2}$ ,  $C_{2@8} = C_{2@1}$ ,  $C_{2@9} = C_{2@6}$ ,  $C_{2@10} = C_{2@5}$ ,  $C_{2@11} =$

$C_{2@3}$ ,  $C_{2@12} = C_{2@4}$  in Fig. 1). The two-fold rotational axes of  $C_{2@1}$ ,  $C_{2@2}$ ,  $C_{2@3}$ ,  $C_{2@4}$ ,  $C_{2@5}$  and  $C_{2@6}$  are along  $(0,1,1)$ ,  $(1,1,0)$ ,  $(1,0,1)$ ,  $(1,-1,0)$ ,  $(0,1,-1)$ , and  $(1,0,-1)$  directions in the cubic unit cell.<sup>5,17</sup> By these  $C_2$  rotations,

a form of the exchange interaction between a pair of nearest neighboring Ir pseudo-spin doublets determines all the others;

$$H = \sum_{\langle i,j \rangle} \begin{pmatrix} S_{i,\mu} & S_{i,\nu} & S_{i,\rho} \end{pmatrix} \begin{pmatrix} J_1 & G_{12} + D_{12} & G_{31} + D_{31} \\ G_{12} - D_{12} & J_2 & G_{23} + D_{23} \\ G_{31} - D_{31} & G_{23} - D_{23} & J_3 \end{pmatrix} \begin{pmatrix} S_{j,\mu} \\ S_{j,\nu} \\ S_{j,\rho} \end{pmatrix}, \quad (1)$$

with

$$\begin{pmatrix} S_{i(j),\mu} & S_{i(j),\nu} & S_{i(j),\rho} \end{pmatrix} = \begin{cases} \begin{pmatrix} S_{i(j),x} & \pm S_{i(j),y} & S_{i(j),z} \\ S_{i(j),z} & \pm S_{i(j),x} & S_{i(j),y} \\ S_{i(j),y} & \pm S_{i(j),z} & S_{i(j),x} \end{pmatrix} & \text{for } \langle i,j \rangle = \langle 1,2 \rangle, \langle 10,12 \rangle, \\ \begin{pmatrix} S_{i(j),z} & \pm S_{i(j),x} & S_{i(j),y} \\ S_{i(j),y} & \pm S_{i(j),z} & S_{i(j),x} \\ S_{i(j),x} & \pm S_{i(j),y} & S_{i(j),z} \end{pmatrix} & \text{for } \langle i,j \rangle = \langle 2,3 \rangle, \langle 4,9 \rangle, \\ \begin{pmatrix} S_{i(j),y} & \pm S_{i(j),z} & S_{i(j),x} \\ S_{i(j),z} & \pm S_{i(j),x} & S_{i(j),y} \\ S_{i(j),x} & \pm S_{i(j),y} & S_{i(j),z} \end{pmatrix} & \text{for } \langle i,j \rangle = \langle 3,1 \rangle, \langle 6,5 \rangle, \\ \begin{pmatrix} \pm S_{i(j),z} & \mp S_{i(j),y} & S_{i(j),x} \\ S_{i(j),y} & S_{i(j),x} & \mp S_{i(j),z} \\ S_{i(j),x} & \pm S_{i(j),z} & \mp S_{i(j),y} \end{pmatrix} & \text{for } \langle i,j \rangle = \langle 7,8 \rangle, \langle 12,1 \rangle, \\ \begin{pmatrix} \pm S_{i(j),z} & \mp S_{i(j),y} & S_{i(j),x} \\ S_{i(j),y} & S_{i(j),x} & \mp S_{i(j),z} \\ S_{i(j),x} & \pm S_{i(j),z} & \mp S_{i(j),y} \end{pmatrix} & \text{for } \langle i,j \rangle = \langle 4,5 \rangle, \langle 2,10 \rangle, \\ \begin{pmatrix} S_{i(j),y} & S_{i(j),x} & \mp S_{i(j),z} \\ S_{i(j),x} & \pm S_{i(j),z} & \mp S_{i(j),y} \\ \mp S_{i(j),y} & \pm S_{i(j),x} & S_{i(j),z} \end{pmatrix} & \text{for } \langle i,j \rangle = \langle 9,2 \rangle, \langle 11,7 \rangle, \\ \begin{pmatrix} S_{i(j),x} & \pm S_{i(j),z} & \mp S_{i(j),y} \\ \mp S_{i(j),y} & \pm S_{i(j),x} & S_{i(j),z} \\ \mp S_{i(j),x} & S_{i(j),y} & \pm S_{i(j),z} \end{pmatrix} & \text{for } \langle i,j \rangle = \langle 5,3 \rangle, \langle 10,9 \rangle, \\ \begin{pmatrix} \mp S_{i(j),y} & \pm S_{i(j),x} & S_{i(j),z} \\ \mp S_{i(j),x} & S_{i(j),y} & \pm S_{i(j),z} \\ \mp S_{i(j),z} & S_{i(j),x} & \pm S_{i(j),y} \end{pmatrix} & \text{for } \langle i,j \rangle = \langle 3,4 \rangle, \langle 6,12 \rangle, \\ \begin{pmatrix} \mp S_{i(j),x} & S_{i(j),y} & \pm S_{i(j),z} \\ \mp S_{i(j),z} & S_{i(j),x} & \pm S_{i(j),y} \\ \pm S_{i(j),y} & S_{i(j),z} & \mp S_{i(j),x} \end{pmatrix} & \text{for } \langle i,j \rangle = \langle 8,4 \rangle, \langle 5,7 \rangle, \\ \begin{pmatrix} \mp S_{i(j),z} & S_{i(j),x} & \pm S_{i(j),y} \\ \pm S_{i(j),y} & S_{i(j),z} & \mp S_{i(j),x} \\ \mp S_{i(j),x} & S_{i(j),y} & \pm S_{i(j),z} \end{pmatrix} & \text{for } \langle i,j \rangle = \langle 7,6 \rangle, \langle 12,11 \rangle, \\ \begin{pmatrix} \pm S_{i(j),y} & S_{i(j),z} & \mp S_{i(j),x} \\ \mp S_{i(j),x} & S_{i(j),y} & \pm S_{i(j),z} \\ \mp S_{i(j),z} & S_{i(j),x} & \pm S_{i(j),y} \end{pmatrix} & \text{for } \langle i,j \rangle = \langle 9,8 \rangle, \langle 11,10 \rangle, \\ \begin{pmatrix} \mp S_{i(j),x} & S_{i(j),z} & S_{i(j),y} \end{pmatrix} & \text{for } \langle i,j \rangle = \langle 1,6 \rangle, \langle 8,11 \rangle, \end{cases}$$

$i, j = 1, \dots, 12$  the sublattice index and the summation of  $\langle i, j \rangle$  is taken over all the nearest neighbor Ir sites. The exchange spin interaction takes the 3 by 3 real-valued matrix form, containing both symmetric ( $J_i$  and  $G_{ij}$ )

and antisymmetric component ( $D_{ij}$ ).

Quantitatively, spin anisotropy in hyperkagome iridate is determined by relative strength between the atomic spin-orbit interaction and non-cubic crystal field splitting among  $t_{2g}$  orbitals.<sup>5</sup> In the larger spin-orbit coupling case,  $J_{\text{eff}} = \frac{1}{2}$  doublet respects the cubic symmetry of the crystal field.<sup>2-5</sup> To reduce a number of the spin-model parameters in eq. (1), we will further postulate the cubic symmetry of the crystal field as well as several additional symmetries which are nearly respected by the lattice parameters of Na-438.

To this end, note first that a form of the quadratic spin Hamiltonian between nearest neighboring Ir pseudo-spin doublets (for clarity of the explanation, choose Ir1 and Ir2 in Fig. 1 henceforth) is mostly determined by direct transfer integral between the two doublets and indirect transfer integrals mediated by oxygen  $p$  orbitals neighboring to the two doublets (O1 and O2 in Fig. 2). An electronic Hamiltonian for these four (Ir1, Ir2, O1 and O2 in Fig. 2) is given by

$$\begin{aligned} H^{\text{el}} = & \epsilon_{\text{Ir},d} \sum_{j=\text{Ir1}, \text{Ir2}, \sigma} f_{j,\sigma}^\dagger f_{j,\sigma} + \sum_{m=\text{O1}, \text{O2}, \sigma} \epsilon_{m,p} \sum_{a=x,y,z} p_{m,a,\sigma}^\dagger p_{m,a,\sigma} + \sum_{i,j=\text{Ir1}, \text{Ir2}, \sigma, \sigma'} t_{ij,\sigma\sigma'} f_{i,\sigma}^\dagger f_{j,\sigma'} \\ & + \sum_{i=\text{Ir1}, \text{Ir2}, m=\text{O1}, \text{O2}, \sigma, \sigma'} \left[ s_{im,a,\sigma\sigma'} f_{i,\sigma}^\dagger p_{m,a,\sigma'} + \text{H.c.} \right] + U_d \sum_{j=\text{Ir1}, \text{Ir2}, \sigma, \sigma'} f_{j,\sigma}^\dagger f_{j,\sigma'}^\dagger f_{j,\sigma'} f_{j,\sigma} \\ & + \sum_{m=\text{O1}, \text{O2}, a,b=x,y,z,\sigma,\sigma'} U_{m,ab} p_{m,b,\sigma}^\dagger p_{m,a,\sigma'}^\dagger p_{m,a,\sigma'} p_{m,b,\sigma} \\ & + \sum_{i=\text{Ir1}, \text{Ir2}, m=\text{O1}, \text{O2}, a=x,y,z,\sigma,\sigma'} U_{m,dp} p_{m,a,\sigma}^\dagger f_{i,\sigma'}^\dagger f_{i,\sigma'} p_{m,a,\sigma} \end{aligned} \quad (2)$$

where  $J_{\text{eff}} = \frac{1}{2}$  pseudo-spin doublet respects the cubic symmetry,<sup>2-5</sup>

$$f_{j,\pm} = \frac{1}{\sqrt{3}} \left\{ \pm i d_{j,xz,s_{\frac{1}{2}}} \mp d_{j,yz,s_{\frac{1}{2}}} \pm d_{j,xy,s_{\frac{1}{2}}} \right\}. \quad (3)$$

$\epsilon_{\text{Om},p}$  is an effective atomic energy for the oxygen  $\text{Om}$  ( $m = 1, 2$ ) and we assume that three  $p$ -orbitals at the re-

spective oxygen  $\text{Om}$  take the same atomic energy, while  $\epsilon_{\text{O1},p} \neq \epsilon_{\text{O2},p}$ .  $s_{im,a,\sigma\sigma'}$  stands for the transfer between the Ir doublet at  $i = \text{Ir1}$  or  $\text{Ir2}$  and the neighboring oxygen  $p$ -orbital ( $a = x, y, z$ ) at  $m = \text{O1}$  or  $\text{O2}$ .  $\sigma(\sigma')$  is the pseudo-spin index.  $t_{ij,\sigma\sigma'}$  is the transfer between two nearest neighbor Ir doublets ( $i, j = \text{Ir1}$  and  $\text{Ir2}$ ).  $U_d$ ,  $U_{m,ab}$  and,  $U_{m,dp}$  denote the on-site Coulomb in-

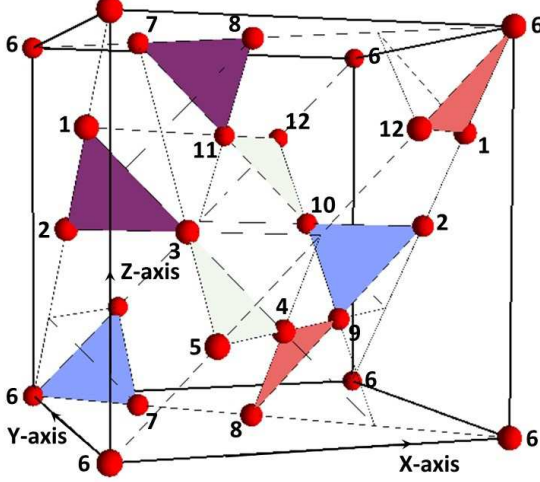


FIG. 1: Cubic unit cell of the hyperkagome lattice, where red sphere stands for iridium atom. The cubic unit cell contains 12 inequivalent iridium sites.

teraction within Ir site, the on-site Coulomb interaction among three  $p$  orbitals within  $O_m$  oxygen site and inter-site Coulomb interaction between Ir site and  $O_m$  oxygen site respectively. Based on the strong coupling expansion, the exchange interaction between two Ir  $J = \frac{1}{2}$  pseudospin doublets is derived from eq. (2).

By way of  $s_{im,a,\sigma\sigma'}$  and  $t_{ij,\sigma\sigma'}$  in eq. (2), the form of the spin interaction between Ir1 and Ir2 is constrained by those *additional* spatial symmetries *applied only for* Ir1, Ir2, O1 and O2. A lattice parameter of Na-438<sup>17</sup> dictates that these four nearly respect two symmetries; one is a bond-centered mirror symmetry (Fig. 2(b)) and the other is bond-centered  $C_2$  rotational symmetry (Fig. 2(c)). The mirror symmetry restricts the Dzyaloshinskii-Moriya (DM) vector to be in the mirror plane, while the  $C_2$  rotation constrains the DM vector to be perpendicular to the  $C_2$  rotational axis. When the two Ir doublets are chosen at Ir1 and Ir2 in Fig. 1, the  $C_2$  rotational axis is along (0, 1, 1) and the mirror plane is perpendicular to the (0, 1, -1), so that the DM interaction vector between Ir1 and Ir2 is along (1, 0, 0), i.e.  $D_{12} = D_{31} = 0$  in eq. (1). Likewise, the symmetric part of the anisotropic exchange interaction between Ir1 and Ir2 respects  $G_{12} = G_{31} = 0$  and  $J_2 = J_3$  due to these two approximate symmetries. Without any justification, we further assume  $G_{23}$  in eq. (1) to be zero. This leads to the following reduced spin Hamiltonian for the hyperkagome iridate;

$$H = \sum_{\langle i,j \rangle} \begin{pmatrix} S_{i,\mu} \\ S_{i,\nu} \\ S_{i,\rho} \end{pmatrix}^T \begin{pmatrix} J+G & 0 & 0 \\ 0 & J-G & D \\ 0 & -D & J-G \end{pmatrix} \begin{pmatrix} S_{j,\mu} \\ S_{j,\nu} \\ S_{j,\rho} \end{pmatrix}, \quad (4)$$

where  $(S_{i(j),\mu}, S_{i(j),\nu}, S_{i(j),\rho})$  follows the same convention as above. This simplified spin model approximately in-

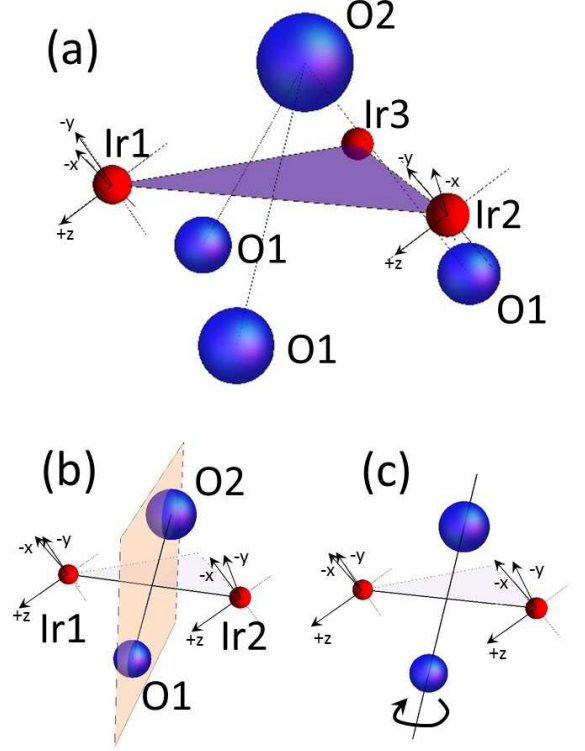


FIG. 2: (a) A triangle formed by three neighboring iridium sites (red spheres; Ir1, Ir2 and Ir3 in Fig. 1) and their neighboring oxygens (blue spheres; three O1 and one O2). O1 is shared by two of three oxygen octahedra whose center accommodate Ir1, Ir2, and Ir3 respectively. O2 is shared by the three oxygen octahedra. Cubic coordinates ( $x, y, z$  coordinates) with which an expression for the  $J = \frac{1}{2}$  doublet, eq. (3), is defined are depicted by black solid lines with arrows at the iridium sites. (b) Bond-centered mirror operation and (c) bond-centered  $C_2$  rotation, under which Ir1 and Ir2 are exchanged with each other, while O1 and O2 remain intact. The lattice parameters of the hyperkagome iridate<sup>17</sup> suggests that spatial coordinates of O1, O2, Ir1, Ir2 and their cubic coordinates nearly respect these two symmetries.

cludes all the effective spin exchange models previously derived.<sup>5,27,28</sup> The actual values of  $J$ ,  $D$  and  $G$  depend on detailed electronic band structure or assumptions. From the high-temperature expansion of eq. (4), the Curie-Weiss temperature for polycrystalline samples is given by  $3J - G$ . From experimental Curie-Weiss fittings of the magnetic susceptibility of powder samples<sup>17-19</sup>, we focus only on  $3J > G$  region.

### III. MONTE CARLO SIMULATION

Monte Carlo (MC) simulation was carried out for a  $12 \times L^3$  spin cluster of the hyperkagome lattice with periodic boundary condition ( $L = 6, \dots, 10$ ). We used

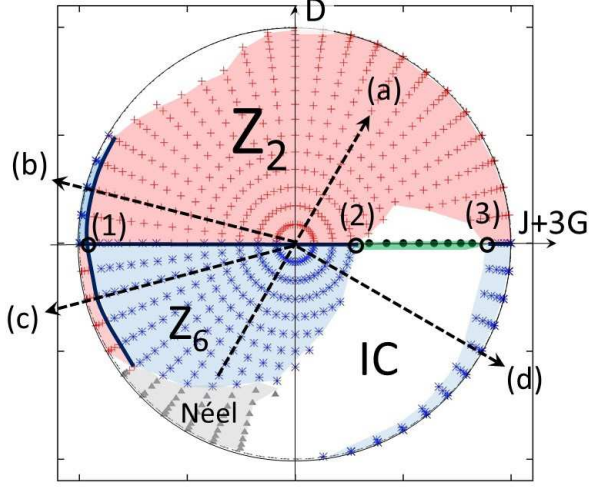


FIG. 3: Low-temperature magnetic phase diagram in  $3J - G > 0$  ( $T = 0.03$ ).  $Z_2$  phase (red cross points)  $Z_6$  phases (blue double cross points), ferrimagnetic phase (green region with black filled circle points), Neel phase (grey triangle points), and incommensurate (IC) magnetic phase (white region). Three open circles at  $D = 0$  (labeled as (1,2,3)) denote high symmetric parameter points; (1) a SU(2) point;  $(J, D, G) = (0, 0, -1)$ , (2) AF Heisenberg point;  $(1, 0, 0)$ , and (3) AF Kitaev point;  $(\frac{1}{\sqrt{2}}, 0, \frac{1}{\sqrt{2}})$ . Four finite- $T$  phase diagrams in Fig. 4 (a,b,c,d) are along four arrows with black broken lines labelled as (a,b,c,d) in Fig. 3 respectively.

the Metropolis method combined with an over-relaxation (microcanonical) update, where 1 MC step comprises of  $12 \times L^3$  number of single-spin flip trials followed by one or two (non-random) sequential applications of microcanonical update<sup>24,29,30</sup>. To increase an acceptance rate of the single-spin flip trial, we impose maximum variation of spin to be smaller for lower temperature,  $|\Delta \mathbf{S}| < T$  (the temperature unit is the square root of  $J^2 + D^2 + G^2$ ). The microcanonical update comprises of a  $\pi$ -rotation of single spin around local exchange field created by its four neighboring spins. We apply the  $\pi$ -rotation on all the spins in sequence. After 30000  $\sim$  40000 MC steps for the thermal equilibration, physical quantities are measured once per every 5 MC steps. Physical quantities are typically averaged over 20000  $\sim$  40000 samples.

Fig. 3 and Fig. 4 show low- $T$  and finite- $T$  magnetic phase diagrams obtained from the simulation. The low- $T$  diagram comprises of  $Z_2$ ,  $Z_6$ ,  $Z_8$  non-coplanar antiferromagnetic phases and non-coplanar ferrimagnetic phase, all of which are associated with  $\mathbf{k} = 0$  ordering, Neel phase with  $\mathbf{k} = (0, \pi, \pi)$  and incommensurate magnetic (IC) phase with  $\mathbf{k} = (\alpha, \alpha, \alpha)$  with  $0 < \alpha < \pi$ . The MC simulation does not see any magnetic orderings up to  $T = 0.03$  at the two high symmetry parameter points; antiferromagnetic (AF) Kitaev point ( $J = G > 0, D = 0$ ) and isotropic AF Heisenberg point ( $J > 0, G = D = 0$ ); see appendix A.<sup>21,24</sup>

$Z_2$  and  $Z_6$  SB magnetic phases and their stabilities

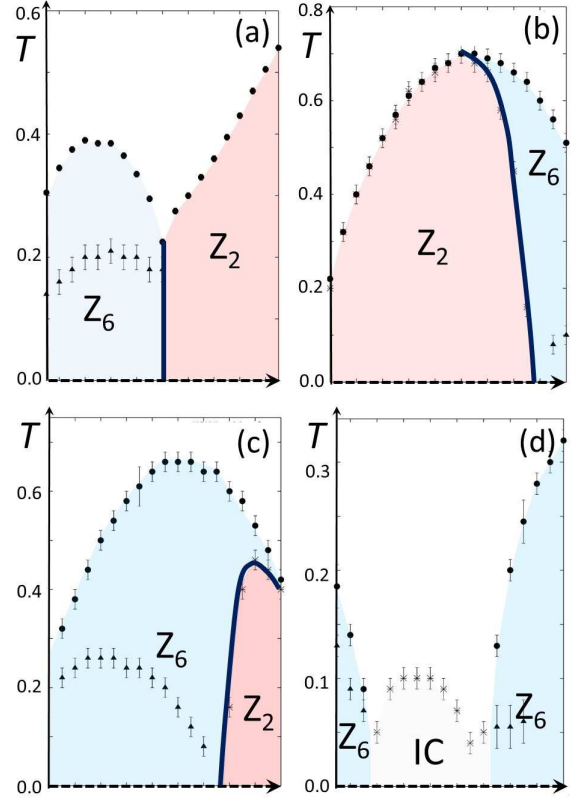


FIG. 4: Finite- $T$  phase diagrams along the broken lines in Fig. 3. Critical temperatures ( $T_c$ ) for  $Z_2$ ,  $Z_6$  SB phase and IC phase are all identified with specific heat peak temperatures (black filled circle points). The crossover temperature ( $T_*$ ) within the  $Z_6$  phase is depicted by black upper triangle points. Phase boundary between  $Z_6$  and  $Z_2$  phases (depicted by bold purple lines) is of the first order with  $Z_8$ -like symmetry (Appendix C).

can be captured by the Luttinger-Tisza (LT) analysis.<sup>31,32</sup> The analysis begins with the Fourier series of the quadratic spin Hamiltonian;

$$H = \sum [\mathbf{H}(\mathbf{k})]_{(j,\alpha|m,\beta)} S_{j,\alpha}(\mathbf{k}) S_{m,\beta}(-\mathbf{k}) \quad (5)$$

with  $j, m$  sublattice index ( $j, m = 1, \dots, 12$ ) and  $\alpha, \beta$  spin index. Spin ordering in a magnetic ground state is specified by a lowest eigenmode of the 36 by 36 Hermitian matrix  $\mathbf{H}(\mathbf{k})$ , provided that the eigenmode is real-valued and satisfies a fixed norm condition. The fixed norm condition requires that the norm over spin index is same for different sublattices. A magnetic structure of the  $Z_2$  phase is given by the lowest eigenmode of  $\mathbf{H}(\mathbf{k})$  at  $\mathbf{k} = 0$ , in which spin moment is ordered transverse to the  $C_2$  rotational axis at respective site. The  $Z_2$  magnetic phase is essentially same as the so-called ‘canted windmill phase’ discussed in a previous work<sup>5</sup>.

The  $Z_6$  SB magnetic phase is characterized by the doubly degenerate eigenmodes at  $\mathbf{k} = 0$  ( $|\phi_1\rangle$  and  $|\phi_2\rangle$ ), which form the 2D irreducible representation of  $\mathbf{H}(\mathbf{k}) =$



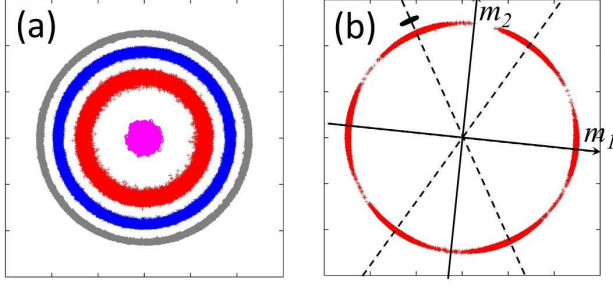


FIG. 5: Distribution of  $(m_1, m_2)$  measured at different temperature and at  $(J, D, G) = (0.50, -0.22, -0.84)$  with  $L = 9$ . (a)  $T > T_*$  ( $T = 0.8$  (pink),  $0.64$  (red),  $0.52$  (blue),  $0.36$  (grey) from center to outside while  $T_c = 0.691$ ). (b)  $T < T_*$  ( $T = 0.24$  (red),  $0.04$  (black) from center to outside). Six dotted lines with the  $Z_6$  symmetry in (b) specify the easy-axis directions within the 2D plane. We choose  $(J, D, G) = (0.50, -0.22, -0.84)$ , because this point is proximate to the possible candidate parameter point for Na-438<sup>5</sup>.

0). Any linear combination of these two cannot satisfy the fixed norm condition; moreover, they break the norm condition in the  $U(1)$  symmetric way. Meanwhile the condition on averaged spin moment can be relaxed at finite temperature due to the thermal fluctuation. In fact, the doubly degenerate lowest eigenmodes of  $\mathbf{H}(\mathbf{k})$  appear at  $\mathbf{k} = 0$  in the  $Z_6$  phase region, and spins become condensed into a plane subtended by these two below a critical temperature  $T_c$  (determined by the specific heat peak). Fig. 5 shows a distribution of a projection of the 12 spins onto the 2D plane, i.e.  $(m_1, m_2)$  defined by

$$m_\mu \equiv \frac{1}{N} \sum_{j,\alpha} S_{j,\alpha} \langle j, \alpha | \phi_\mu \rangle, \quad (6)$$

where  $j$  is the site index and  $\alpha$  is the spin index. For  $T > T_c$ , the projection is accumulated at origin ( $\langle \Psi \rangle = 0$  with  $\Psi \equiv m_1 + i m_2$ ). For  $T < T_c$ , the amplitude develops continuously ( $\langle |\Psi| \rangle \neq 0$ ). The simulation on a finite-size system suggests another characteristic temperature  $T_*$  ( $< T_c$ ), above which the distribution has the  $U(1)$  symmetry ( $\langle \theta \rangle$  indefinite with  $\Psi \equiv |\Psi| e^{i\theta}$ ) but below which it acquires an additional  $Z_6$  structure ( $\langle \cos 6\theta \rangle \neq 0$  with  $\Psi \equiv |\Psi| e^{i\theta}$ ).

#### IV. CLASSICAL ORDER BY DISORDER MECHANISM

The  $Z_6$  anisotropy at the lower temperature ( $T < T_*$ ) can be understood from the classical order by disorder mechanism. To see this, let us expand  $\mathbf{H}(\mathbf{k})$  near  $\mathbf{k} = 0$  with respect to small  $\mathbf{k}$  and derive an effective Hamiltonian in the basis of  $|\phi_1\rangle$  and  $|\phi_2\rangle$  using the  $\mathbf{k} \cdot \mathbf{p}$  perturbation. On the second order in  $\mathbf{k}$ , the effective Hamiltonian

in the 2D plane subtended by  $|\phi_1\rangle$  and  $|\phi_2\rangle$  is ;

$$\mathbf{H}_{\text{eff}}^{2 \times 2}(\mathbf{k}) = \epsilon_0 + \hat{\mathbf{V}}_1^{2 \times 2}(\mathbf{k}) + \sum_{n \neq 0} \frac{\mathbf{t}_{0n}(\mathbf{k}) \cdot \mathbf{t}_{n0}(\mathbf{k})}{\epsilon_n - \epsilon_0}.$$

$\epsilon_0$  is the lowest eigenenergy of  $\mathbf{H}(\mathbf{k} = 0)$  to which  $|\phi_1\rangle$  and  $|\phi_2\rangle$  belong to.  $\epsilon_n$  is a higher eigenenergy of  $\mathbf{H}(\mathbf{k} = 0)$ .  $\mathbf{V}_1^{2 \times 2}(\mathbf{k})$  is a 2 by 2 block of  $\Delta \mathbf{H}(\mathbf{k}) \equiv \mathbf{H}(\mathbf{k}) - \mathbf{H}(\mathbf{k} = 0)$  in the basis of  $|\phi_1\rangle$  and  $|\phi_2\rangle$ ;  $[\mathbf{V}_1^{2 \times 2}(\mathbf{k})]_{ij} \equiv \langle \phi_i | \Delta \mathbf{H}(\mathbf{k}) | \phi_j \rangle$ .  $\mathbf{t}_{0n}(\mathbf{k})$  is a 2 by  $N$  block of  $\Delta \mathbf{H}(\mathbf{k})$  which connects  $|\phi_1\rangle$  and  $|\phi_2\rangle$  with the  $N$ -fold degenerate higher energy eigenstates of  $\mathbf{H}(\mathbf{k} = 0)$  belonging to  $\epsilon_n$ ,  $|\phi_m^{(n)}\rangle$  ( $m = 1, \dots, N$ );  $[\mathbf{t}_{0n}(\mathbf{k})]_{im} \equiv \langle \phi_i | \Delta \mathbf{H}(\mathbf{k}) | \phi_m^{(n)} \rangle$ .

A form of the 2 by 2 effective Hamiltonian thus obtained is constrained by the point group symmetry. To see this, note first that, in the 2D irreducible representation of  $\mathbf{H}(\mathbf{k} = 0)$ ,  $C_{2@1} \cdot C_{2@5}$ ,  $C_{2@2} \cdot C_{2@4}$  and  $C_{2@3} \cdot C_{2@6}$  are the identity operation; choosing *any* direction within the 2D plane will not break any of these point group symmetries. These three require that the Hamiltonian is quadratic in small  $\mathbf{k}$ . Namely, these symmetry operations change the sign of  $\mathbf{k}$ ,  $C_{2@1} \cdot C_{2@5}(k_x, k_y, k_z) = (k_x, -k_y, -k_z)$ ,  $C_{2@2} \cdot C_{2@4}(k_x, k_y, k_z) = (-k_x, -k_y, k_z)$  and  $C_{2@3} \cdot C_{2@6}(k_x, k_y, k_z) = (-k_x, k_y, -k_z)$ , while they are identity operation in the 2D plane. Besides,  $\mathbf{H}^*(\mathbf{k}) = \mathbf{H}(-\mathbf{k})$  so that the effective Hamiltonian is real-valued within the second order in  $\mathbf{k}$ . It takes the form of

$$\mathbf{H}_{\text{eff}}^{2 \times 2}(\mathbf{k}) = d_3(\mathbf{k}) \sigma_3 + d_1(\mathbf{k}) \sigma_1 + d_0(\mathbf{k}) \sigma_0 + \mathcal{O}(\mathbf{k}^3) \quad (7)$$

in the basis of  $|\phi_1\rangle$  and  $|\phi_2\rangle$ ;  $\sigma_3 |\phi_{1/2}\rangle = \pm |\phi_{1/2}\rangle$ . Here real-valued  $d_j(\mathbf{k})$  is quadratic in  $\mathbf{k}$ .

On the other hand,  $C_{2@1}$ ,  $C_{2@2}$  and  $C_{2@3}$  are mirror operations in the 2D plane, where respective mirror axes form 60 degree angle against one another. Let us call a mirror axis of  $C_{2@1}$  to be along  $|\phi_2\rangle$  and call its orthogonal vector as  $|\phi_1\rangle$ . In this basis, three operations are represented by;

$$C_{2@1} = \begin{pmatrix} -1 & 0 \\ 0 & 1 \end{pmatrix}, \quad C_{2@2} = \begin{pmatrix} \frac{1}{2} & \frac{\sqrt{3}}{2} \\ \frac{\sqrt{3}}{2} & -\frac{1}{2} \end{pmatrix}, \\ C_{2@3} = \begin{pmatrix} \frac{1}{2} & -\frac{\sqrt{3}}{2} \\ -\frac{\sqrt{3}}{2} & -\frac{1}{2} \end{pmatrix}.$$

These mirror symmetries constrain the form of  $d_j(\mathbf{k})$  in eq. (7);

$$C_{2@1} \cdot \mathbf{H}_{\text{eff}}^{2 \times 2}(k_x, k_y, k_z) \cdot C_{2@1} = \mathbf{H}_{\text{eff}}^{2 \times 2}(-k_x, k_z, k_y), \\ C_{2@2} \cdot \mathbf{H}_{\text{eff}}^{2 \times 2}(k_x, k_y, k_z) \cdot C_{2@2} = \mathbf{H}_{\text{eff}}^{2 \times 2}(k_y, k_x, -k_z), \\ C_{2@3} \cdot \mathbf{H}_{\text{eff}}^{2 \times 2}(k_x, k_y, k_z) \cdot C_{2@3} = \mathbf{H}_{\text{eff}}^{2 \times 2}(k_z, -k_y, k_x).$$

These three conditions give out

$$\mathbf{H}_{\text{eff}}^{2 \times 2}(\mathbf{k}) = k^2 \left\{ d(-2\hat{k}_x^2 + \hat{k}_y^2 + \hat{k}_z^2) \sigma_3 - \sqrt{3}d(\hat{k}_y^2 - \hat{k}_z^2) \sigma_1 + A \sigma_0 \right\} + \mathcal{O}(k^3), \quad (8)$$

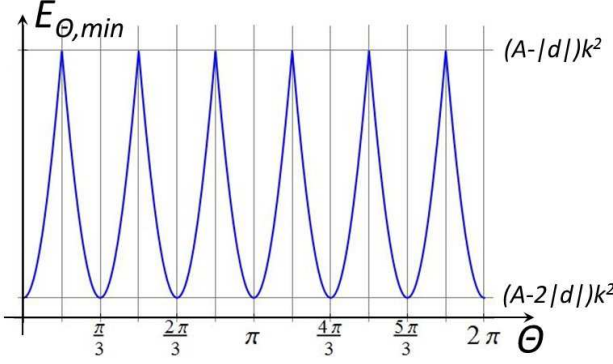


FIG. 6: The lowest magnetic energy of finite-momentum spin configuration around  $|\theta\rangle \equiv \cos\theta|\phi_1\rangle + \sin\theta|\phi_2\rangle$  is shown as a function of  $\theta$  for  $d > 0$ . The vertical axis denotes  $E_{\theta, \min} \equiv \min_{\mathbf{k}} E_{\theta, \mathbf{k}}$  with  $E_{\theta, \mathbf{k}} \equiv \langle \theta | \mathbf{H}_{\text{eff}}^{2 \times 2}(\mathbf{k}) | \theta \rangle$ .

with  $k \equiv |\mathbf{k}|$  and  $\hat{k} \equiv \mathbf{k}/k$ . Here  $d$  and  $A(> 2|d|)$  depend on a microscopic parameter. They satisfy  $A - 2|d| > 0$  in the  $Z_6$  phase region, where the lowest eigenmodes of  $\mathbf{H}(\mathbf{k})$  are at  $\mathbf{k} = 0$ .

A magnetic energy for a linear combination of  $|\phi_1\rangle$  and  $|\phi_2\rangle$  with finite (but small) momenta can be calculated from  $\mathbf{H}_{\text{eff}}^{2 \times 2}(\mathbf{k})$  as  $E_{\theta, \mathbf{k}} \equiv \langle \theta | \mathbf{H}_{\text{eff}}^{2 \times 2}(\mathbf{k}) | \theta \rangle$  with  $|\theta\rangle \equiv \cos\theta|\phi_1\rangle + \sin\theta|\phi_2\rangle$ . The energy for such a spin configuration can be further minimized with respect to  $\hat{k}$ . The minimized energy has 6 minima at  $\theta = 0, \pm\frac{\pi}{3}, \pm\frac{2\pi}{3}, \pi$  for  $d > 0$ , while at  $\theta = \pm\frac{\pi}{6}, \pm\frac{\pi}{2}, \pm\frac{5\pi}{6}$  for  $d < 0$  (Fig. 6). The optimal directions of  $\hat{k}$  for the former 6 minima are along  $k_z, k_x(k_y), k_y(k_x), k_z$  axes respectively. Due to the entropy effect, either one of these two types of six minima is selected as the ordering direction at finite temperature.

To see this entropy effect, one can also calculate the free energy which includes spatial fluctuation around  $|\theta\rangle$  within the second order in small  $\mathbf{k}$ ;

$$F(\theta) = -\frac{1}{\beta} \ln \frac{1}{V} \sum_{\mathbf{k}} e^{-\beta E_{\theta, \mathbf{k}}} = \frac{1}{2\beta} \ln \left[ \prod_{j=x,y,z} (4\pi\beta B_j) \right]$$

with  $B_x \equiv A - 2d \cos 2\theta$ ,  $B_y \equiv A - 2d \cos(2\theta - \frac{2\pi}{3})$  and  $B_z \equiv A - 2d \cos(2\theta + \frac{2\pi}{3})$ . At  $T \neq 0$ ,  $F(\theta)$  has indeed six minima at  $\theta = 0, \pm\frac{\pi}{3}, \pm\frac{2\pi}{3}, \pi$  for  $d > 0$ , while at  $\theta = \pm\frac{\pi}{6}, \pm\frac{\pi}{2}, \pm\frac{5\pi}{6}$  for  $d < 0$ . Consistently, the MC simulation found that the system at the lower temperature prefers either one of these two types of six minima (Fig. 5(b)).

When  $|\phi_1\rangle$  (or its 5 counterparts;  $\theta = 0, \pm\frac{\pi}{3}, \pm\frac{2\pi}{3}$ ) is selected by the classical order by disorder, the spin configuration breaks all  $C_{2@j}$  ( $j = 1, 2, 3$ ) but is invariant under  $C_{2@1} \cdot T$ ; the generator of the reduced magnetic point group is  $\{C_{2@1} \cdot C_{2@5}, C_{2@2} \cdot C_{2@4}, C_{2@3} \cdot C_{2@6}, C_{2@1} \cdot T\}$ . The first three in the set change the sign of spin moments, i.e.  $C_{2@1} \cdot C_{2@5} (S_x, S_y, S_z) = (S_x, -S_y, -S_z)$ ,  $C_{2@2} \cdot C_{2@4} (S_x, S_y, S_z) = (-S_x, -S_y, S_z)$  and  $C_{2@3} \cdot C_{2@6} (S_x, S_y, S_z) = (-S_x, S_y, -S_z)$ . Thus, the phase

is an antiferromagnetic (AF) phase without any finite off-diagonal elements of magnetic susceptibility tensor;  $\chi_{xy} = \chi_{yz} = \chi_{zx} = 0$ . The last one in the set,  $C_{2@1} \cdot T$ , connects  $y$  and  $z$  while it connects  $x$  with neither  $y$  nor  $z$ ; the phase shows spin anisotropy in diagonal susceptibility,

$$\chi_{xx} \neq \chi_{yy} = \chi_{zz}. \quad (9)$$

When  $|\phi_2\rangle$  (or its 5 counterparts;  $\theta = \pm\frac{\pi}{2}, \pm\frac{\pi}{6}, \pm\frac{5\pi}{6}$ ) is chosen, the configuration breaks  $C_{2@2}$  and  $C_{2@3}$ , but is invariant under  $C_{2@1}$ ;  $\{C_{2@1} \cdot C_{2@5}, C_{2@2} \cdot C_{2@4}, C_{2@3} \cdot C_{2@6}, C_{2@1}\}$ . Accordingly, the phase is an AF phase without off-diagonal susceptibility tensor and with  $\chi_{xx} \neq \chi_{yy} = \chi_{zz}$ . In the presence of large lattice-spin coupling, both of these two  $Z_6$  SB phases are accompanied with an uniaxial lattice distortion differentiating  $x$  coordinate from  $y$  and  $z$  coordinates.

## V. EMERGENT $U(1)$ SYMMETRY AROUND THE CRITICAL POINT

The  $U(1)$  to  $Z_6$  crossover behavior around  $T_*$  in the  $Z_6$  SB magnetic phase can be crudely captured by the six states ferromagnetic Potts model in the 3D lattice. Low- $T$  physics of the Potts model are controlled by 3D XY fixed point,  $T = 0$  Nambu-Goldstone (NG) fixed point and  $T = 0$  fixed point with large  $Z_6$  term.<sup>33,34</sup> The critical point ( $T = T_c$ ) belongs to the XY fixed point, below which all the renormalization group (RG) flow goes to the large  $Z_6$  fixed point.<sup>33</sup> The  $U(1)$  to  $Z_6$  crossover below  $T_c$  stems from the dangerously irrelevant behavior of the  $Z_6$  anisotropy term.<sup>33,34</sup> The anisotropy term is renormalized to smaller value around the XY fixed point, while it blows up into larger value around the NG fixed point. Due to this behavior, a smaller system near  $T_c$  behaves as if it has much reduced  $Z_6$  anisotropy, while a larger system far from  $T_c$  behaves as a system with enhanced anisotropy.

Fig. 7 shows a set of temperature dependencies of the XY order parameter and  $Z_6$  order parameter;

$$m^2 \equiv m_1^2 + m_2^2 \\ m_6 \equiv [(m_1 + im_2)^6 + (m_1 - im_2)^6]/(2m^5),$$

calculated for different system sizes ( $L = 5, 6, 7, 8, 9, (10)$ ) at two different parameter points in the  $Z_6$  SB phase region;  $(J, D, G) = (0.50, -0.22, -0.84)$  and  $(0.69, -0.53, -0.50)$ . The  $T$ -dependences of  $m$  and  $m_6$  clearly show that, in finite system sizes, the XY order parameter and the  $Z_6$  order parameter start to take finite values at different temperatures. Note also that the former parameter point is proximate to the  $SU(2)$  symmetry point  $(J, D, G) = (0, 0, -1)$ ; the  $SU(2)$  point is approximately an effective spin model of Na-438, when the atomic spin-orbit interaction is larger than the non-cubic crystal field splitting energy and when the exchange path is mainly mediated by the oxygen ions<sup>5</sup>. Meanwhile, the

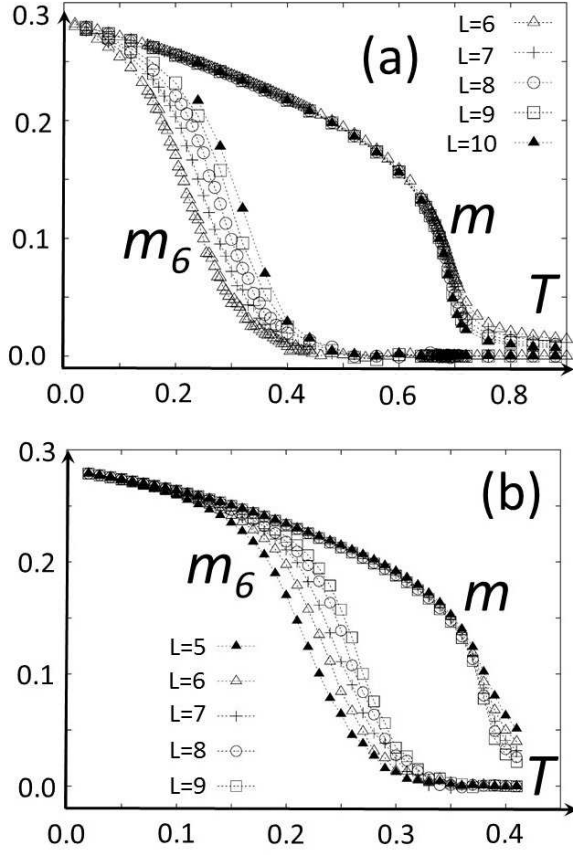


FIG. 7: Temperature dependence of XY order parameter  $m$  and  $Z_6$  SB order parameter ( $m_6$ ) at different parameter points; (a)  $(J, D, G) = (0.50, -0.22, -0.84)$  (b)  $(J, D, G) = (0.69, -0.53, -0.50)$ .

latter parameter point is far from any high symmetric parameter points, playing the role of a good reference parameter point (see below).

The crossover system size and temperature can be evaluated from the FNS analysis on the XY order parameter  $m$  and  $Z_6$  order parameter  $m_6$ . The scaling argument<sup>34–36</sup> suggests that these two follow single-parameter scalings;

$$m = L^{-\sigma} f(tL^{1/\nu}), \quad (10)$$

$$m_6 = L^{-\sigma} f_6(tL^{1/\nu_6}), \quad (11)$$

with  $\sigma = \beta/\nu$  and  $t \equiv |T - T_c|/T_c$ .  $\beta$  and  $\nu$  denote the critical exponents of the 3D XY universality class. Fig. 8 and 9 show respective one-parameter scaling fittings at the two parameter points. To obtain them, we fixed the critical exponents  $\beta$  and  $\nu$  to be those for the 3D XY universality class ( $\nu = 0.672$  and  $\beta = 0.348$ )<sup>37</sup>, while fine-tuned the critical temperature  $T_c$  such that all the data points for  $m$  fall into one scaling function  $f(x)$ . With  $T_c$  thus obtained, we further fine-tuned the crossover exponent for  $m_6$ ,  $\nu_6$ , such that all the data points for

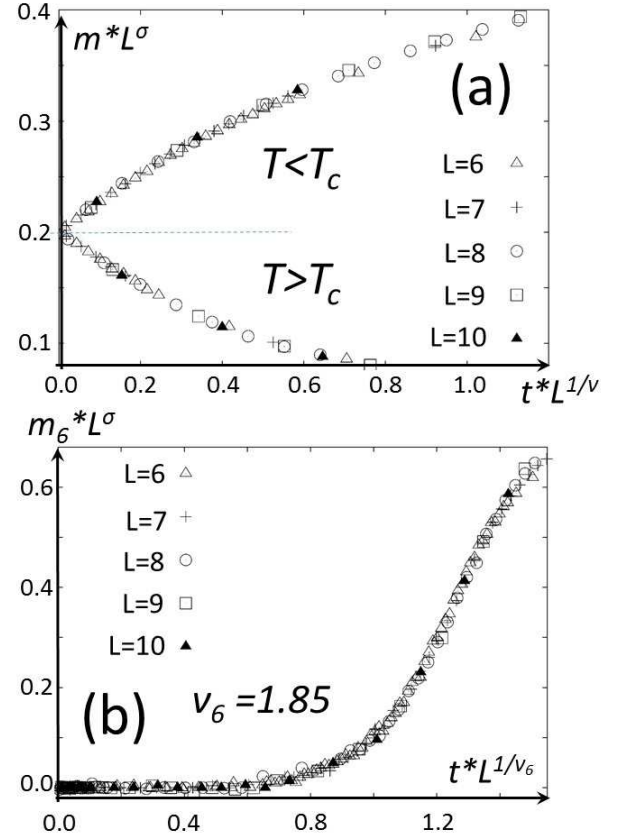


FIG. 8: Single-parameter scalings for XY order parameter  $m$  (a) and  $Z_6$  SB order parameter  $m_6$  (b) at  $(J, D, G) = (0.50, -0.22, -0.84)$ .

$m_6$  fall into the one-parameter scaling function  $f_6(x)$ . The two fittings demonstrate that all the numerical data points for  $m$  and  $m_6$  taken from different system size ( $L = 5, 6, \dots, 10$ ) fall into respective one-parameter scaling functions. The optimal  $\nu_6$  is evaluated at two different parameter points,  $(J, D, G) = (0.69, -0.53, -0.50)$ ,  $(0.50, -0.22, -0.84)$ , as  $1.45 \pm 0.05$  and  $1.85 \pm 0.05$  respectively. The crossover system size  $\Lambda_*$  and temperature  $T_*$  can be obtained by equating the argument of  $f_6(\dots)$  with unit;  $t\Lambda_*^{1/\nu_6} = 1$  or  $t_*\Lambda^{1/\nu_6} = 1$ . With  $\xi \sim t^{-\nu}$ , we obtain  $\Lambda_* \sim \xi^{\nu_6/\nu}$  and  $\Delta T_* \sim \Lambda^{-1/\nu_6}$  respectively.

The former value of the crossover exponent  $\nu_6$  ( $1.45 \pm 0.05$ ) is consistent with previous estimation in the Potts model<sup>35,36</sup>, while the latter value ( $1.85 \pm 0.05$ ) is relatively larger. The discrepancy stems from the presence of a high symmetric point at  $(J, D, G) = (0, 0, -1)$  near the latter parameter point. The symmetric point has a global  $SU(2)$  symmetry toward which the  $Z_6$  anisotropy diminishes. Such a symmetric point plays the role of another crossover fixed point for RG flow, changing the crossover exponent from that of the simple  $Z_6$  Potts model.

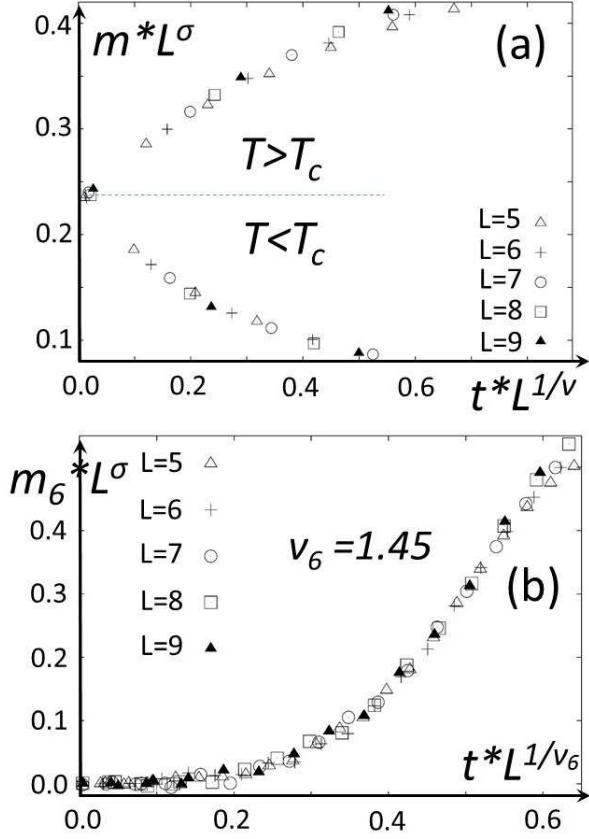


FIG. 9: Single-parameter scalings for the XY order parameter  $m$  (a) and  $Z_6$  order parameter  $m_6$  (b) at  $(J, D, G) = (0.69, -0.53, -0.50)$ .

## VI. EFFECTS OF QUANTUM FLUCTUATION

In the quantum  $J = 1/2$  pseudo-spin case, the techniques used in this paper may not be able to capture physics at or near highly frustrated parameter points, where all magnetic ordering temperatures reduce to zero due to strong spin frustration. Such frustrated points include the AF Heisenberg point  $(J, D, G) = (1, 0, 0)$  and Kitaev point  $(J, D, G) = (\frac{1}{\sqrt{2}}, 0, \frac{1}{\sqrt{2}})$ . On the one hand, a comparison between preceding classical calculations<sup>39,40</sup> and quantum calculations<sup>6,12</sup> on the honeycomb iridate spin model suggests that, even for the quantum  $J = 1/2$  case, physics discussed in this paper may hold true in those parameter regions with higher magnetic ordering temperatures. Such parameter regions cover most of the physically relevant parameter regions ( $3J - G > 0$ ), including one of the ‘candidate’ parameter points, i.e. the SU(2) point  $(J, D, G) = (0, 0, -1)$ . In these regions, the quantum fluctuation changes the results in a quantitative level as discussed below.

Firstly, the  $Z_2$ - $Z_6$  phase boundaries in Fig. 3 at  $T = 0$  are expected to move into the  $Z_2$  phase side due to the quantum fluctuation. This is because the finite- $T$  first or-

der phase boundary between  $Z_2$  and  $Z_6$  phases is slanted in a way that the  $Z_6$  phases are more stabilized against the  $Z_2$  phase by the thermal effect (Fig. 4(b,c)). With the Clausius-Clapeyron relation, this indicates that, around the phase boundary, the  $Z_6$  SB states have more low energy classical spin configurations ‘proximate’ to themselves than the competing  $Z_2$  SB state has. Here we define a given classical spin configuration “ $x$ ” to be more ‘proximate’ to “ $y$ ” than to “ $z$ ” when  $x \cdot y > x \cdot z$ , where “ $\cdot$ ” denotes the inner product between two spin configurations with respect to spin index and site index.

Crudely speaking, the quantum zero-point energy<sup>41</sup> can be regarded as the second-order energy correction to the classical ground state, which comes from the virtual hopping processes between the classical ground state  $|0\rangle$  and another classical spin states with higher classical energies  $|n\rangle$ ;

$$E_{\text{SW}} = - \sum_n \frac{|\langle 0 | H' | n \rangle|^2}{E_n - E_0} + \mathcal{O}(H'^4). \quad (12)$$

Here  $H'$  stands for the quantum fluctuation term, comprising ‘off-diagonal’ terms such as  $a_i^\dagger a_j^\dagger$ ,  $a_i a_j$ , and  $a_i^\dagger a_j$  with  $i \neq j$ , while  $a_i^\dagger$  being the Holstein-Primakoff boson (creation) operator at the  $i$ -th site. The zero-th order part  $H_0$  comprises ‘diagonal’ terms such as  $a_i^\dagger a_i$ , giving the classical energies to each classical spin states e.g.  $H_0 |n\rangle = E_n |n\rangle$ .

The indication of the finite- $T$  phase boundary between  $Z_2$  and  $Z_6$  phases in combination with eq. (12) suggests that, near the  $Z_2$ - $Z_6$  phase boundaries at  $T = 0$  in Fig. 4(b,c), the quantum zero-point energy of the  $Z_6$  states will be larger than that of the  $Z_2$  state. Namely, the  $Z_6$  states have possibly more low-energy classical spin configurations ( $|n\rangle$ ) connecting with  $Z_6$  states by the local perturbation  $H'$  than the  $Z_2$  state does. As a result, the  $Z_2$ - $Z_6$  classical phase boundaries in Fig. 4(b,c) are expected to move into the  $Z_2$  phase side, when the quantum fluctuation is included perturbatively. In fact, one can find in a recent literature<sup>42</sup> a model calculation on a different spin system, whose observation agrees with the thoughts given above. One may also notice from Fig. 4(a) that the finite- $T$  phase boundary between  $Z_2$  and  $Z_6$  phases is constrained in the  $D = 0$  plane. This exceptional feature is, however, due to the additional symmetry at  $D = 0$  (Appendix A).

Another possible quantitative change could be found in the finite-size crossover phenomena in the  $Z_6$  phase, which may be effectively characterized by the  $(d+1)$ -dimensional  $Z_6$  ferromagnetic Potts model. In the effective model, the quantum effect is taken into account as an addition of the imaginary time dimension (+1) to the spatial dimension ( $d = 3$ ). The 4D  $Z_6$  Potts model exhibits the same kind of finite-size crossover phenomena with different crossover exponent<sup>36</sup>. Moreover, in the (3+1)D model, finite temperature leads to a non-trivial ‘finite-size’ effect along the imaginary time direction, in the same way as the finite system size does along the



spatial direction. Thus, one may even expect that the  $Z_6$  ordered phase accommodates two distinct crossover temperatures below a finite critical ordering temperature  $T_c$ ; one is associated with the spatial fluctuation of spins and the other with their temporal fluctuation.

## VII. DISCUSSION

In this paper, we obtained a comprehensive classical magnetic phase diagram for the hyperkagome iridate. We clarified the origin of the  $Z_6$  anisotropy and finite- $T$  ordering nature of the  $Z_6$  phases. Our finite- $T$  classical phase diagram suggests that the  $Z_6$  phases could be further stabilized against the competing  $Z_2$  phase by the quantum order by disorder.

Based on the finite- $T$  crossover behavior in the  $Z_6$  SB phase, let us finally introduce a possible phenomenology of Na-438 powder samples. Firstly we assume that polycrystalline grain size is as small as  $1\mu\text{m} \sim 0.1\mu\text{m}$  and we regard that a broad peak in specific heat observed around  $T \simeq 35\text{K}$  in experiments<sup>17–19</sup> corresponds to the onset temperature of the  $Z_6$  SB phase ( $T_c$ ). The FNS argument above claims that, below but near  $T_c$ , a system smaller than the crossover system size  $\Lambda_* = \xi^{\nu_6/\nu}$  behaves as if it has no  $Z_6$  anisotropy term. Spins in such a small grain collectively develop a finite amplitude of  $\Phi \equiv \phi_1 + i\phi_2$  below  $T_c$ , while the phase of  $\Phi$  still strongly fluctuates and so does that of individual spins. Thus, any local spin moment seen by probe spins can be averaged to be zero in the intermediate temperature regime  $T_* < T < T_c$ . For  $\xi = 3, 5, 7, 10$  cubic unit cells, the crossover system size is evaluated to be  $\Lambda_* = 20, 90, 230, 630$  cubic unit cells for  $\nu_6 = 1.85$  (0.017, 0.08, 0.20, 0.56  $\mu\text{m}$  with  $a=8.95$  Å). On further lowering temperature, the correlation length  $\xi$  becomes shorter and so does  $\Lambda_*$ . When  $\Lambda_*$  exceeds the grain size on lowering temperature ( $T < T_*$ ), the  $Z_6$  anisotropy becomes prominent and the phase of  $\Phi$  starts to be locked into the six minima. As explained above, this locking breaks the point group symmetry, giving rise to the uniaxial lattice distortion via spin-lattice coupling. Since neighboring grains in polycrystalline sample are expected to be randomly oriented against one another, the locking or its onset around  $T_*$  with the uniaxial distortion will conflict with the grain structure. This may result in a ‘configurationally degenerate phase with fluctuating order’ as suggested in the experiment<sup>19</sup>.

The author would like to thank Gang Chen, Kenji Harada and Xuerong Liu for fruitful discussions. This work was financially supported by NBRP of China (2015CB921104).

### Appendix A: Finite- $T$ phase diagram at $D = 0$

Finite- $T$  phase diagrams at  $D = 0$  are shown in Fig. 10. A group of Hamiltonians at  $D = 0$  is symmetric under a ‘Klein’ transformation  $G^{26}$ ;  $H_\theta = G \cdot H_{\frac{\pi}{2}-\theta} \cdot G$

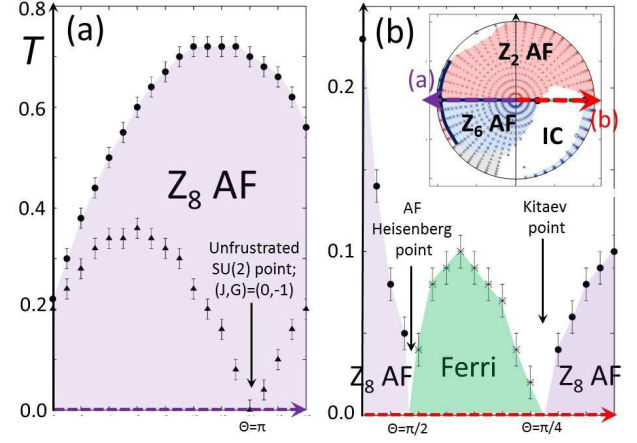


FIG. 10: Finite- $T$  phase diagrams at  $D = 0$  and  $3J - G > 0$ . (a)  $\frac{\pi}{2} + \varphi < \theta < \pi + \varphi$  (b)  $\varphi < \theta < \frac{\pi}{2} + \varphi$  with  $(J, G) = (\sin \theta, \cos \theta)$  and  $\tan \varphi = \frac{1}{3}$ . The critical temperatures of the  $Z_8$  AF phase and ferrimagnetic phase are determined from specific heat peak (black filled circle points and black double crossed points). The crossover temperature within the  $Z_8$  AF phase is determined from temperature dependence of sublattice magnetization (black upper triangle points).

with  $(J, G) \equiv (\sin \theta, \cos \theta)$ . This connects antiferromagnetic (AF) and ferromagnetic (F) Heisenberg point  $(J, G) = (\pm 1, 0)$  with two other symmetric points with global SU(2) symmetries  $(J, G) = (0, \pm 1)$ , while leaves intact AF Kitaev point  $(J, G) = (\frac{1}{\sqrt{2}}, \frac{1}{\sqrt{2}})$  and F Kitaev point  $(J, G) = -(\frac{1}{\sqrt{2}}, \frac{1}{\sqrt{2}})$ . Consistently, the finite- $T$  phase diagram at  $D = 0$  is symmetric under this transformation, where the ferrimagnetic phase ( $\frac{\pi}{4} < \theta < \frac{\pi}{2}$ ) is transformed by  $G$  to the  $Z_8$  antiferromagnetic phase ( $0 < \theta < \frac{\pi}{4}$ ), the ferromagnetic phase ( $-\frac{3\pi}{4} < \theta < 0$ ) to the  $Z_8$  antiferromagnetic phase ( $\frac{\pi}{2} < \theta < \frac{5\pi}{4}$ ). The ordering temperatures of respective phases vanish at two AF SU(2) points ( $\theta = 0, \frac{\pi}{2}$ ) and two Kitaev points ( $\theta = \frac{\pi}{4}, \frac{5\pi}{4}$ ). On the one hand, two F SU(2) points ( $\theta = \pi, \frac{3\pi}{2}$ ) are unfrustrated points, where magnetic orderings show the maximum transition temperature. No O(3) to  $Z_8$  crossover is observed within  $0 < \theta < \frac{\pi}{2}$ , while, for  $\frac{\pi}{2} < \theta < 2\pi$ , O(3) to  $Z_8$  crossover are observed below ordering temperatures for a finite-size system. The crossover region becomes widest at the unfrustrated F SU(2) point.

### Appendix B: finite size scaling analysis in $Z_8$ SB phase

The MC simulation shows that the phase boundary between the  $Z_2$  and  $Z_6$  SB phase is always of the first order (Appendix C), indicating the existence of a bicritical point at finite temperature. Below the bicritical point, the system exhibits  $Z_8$  SB magnetic phase with O(3)-

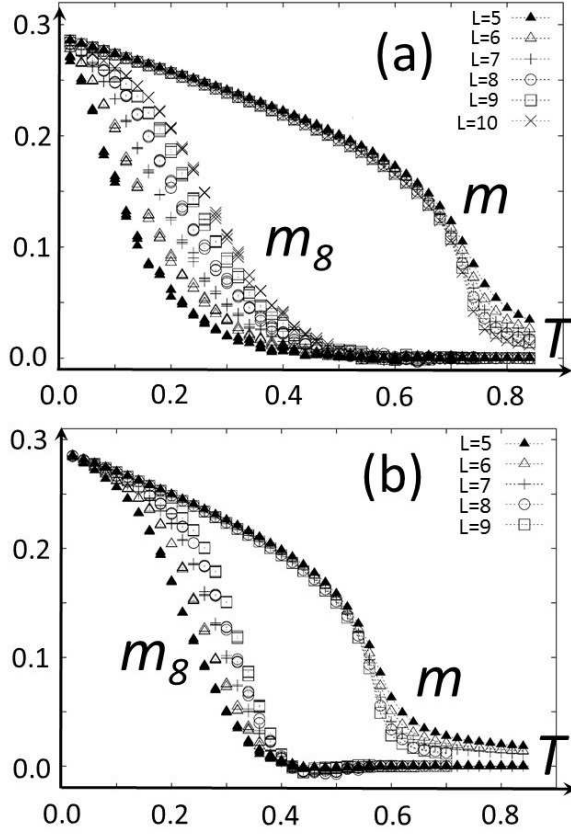


FIG. 11: Temperature dependence of O(3) order parameter  $m$  and  $Z_8$  SB order parameter  $m_8$  at different parameter points; (a)  $(J, D, G) = (0.11, 0.0, -0.99)$  (b)  $(J, D, G) = (0.31, 0.0, -0.95)$ .

type spin fluctuation. This situation can be clearly seen at the phase boundary of  $D = 0$  by the LT analysis. In the phase boundary between  $Z_2$  and  $Z_6$  phases,  $\mathbf{H}(\mathbf{k})$  has triple degeneracy in its lowest eigenmodes at  $\mathbf{k} = 0$ ; two are the doubly degenerate lowest eigenmodes from the  $Z_6$  phase region ( $|\phi_1\rangle$  and  $|\phi_2\rangle$ ) and one is the lowest eigenmode from the  $Z_2$  phase region ( $|\phi_3\rangle$ ). These three form a O(3) sphere in the 36 dimensional space. On the sphere, the fixed norm condition is satisfied only along 8 high-symmetry directions;  $\pm(1, 1, 1)$ ,  $\pm(1, 1, -1)$ ,  $\pm(1, -1, 1)$ ,  $\pm(-1, 1, 1)$  ( $(1, 1, 1)$  means  $|\phi_1\rangle + |\phi_2\rangle + |\phi_3\rangle$ ), while otherwise not in general. These directions become strong easy-axis directions, giving rise to the cubic anisotropy in the O(3) vector model.

The ordering nature of the 3D O( $n$ ) vector model with the cubic anisotropy is determined by either 3D Heisenberg fixed point ( $n < n_c$ ) or cubic fixed point ( $n > n_c$ ). Preceding studies including the fifth order  $4-\epsilon$  expansion conclude that  $n_c$  is smaller than 3 ( $n_c = 2.89$ ).<sup>38</sup> Being consistent with this, the MC simulation on  $G > 0$  and  $D = 0$  region does not observe any O(3) to  $Z_8$  crossover behavior (see Fig. 10(b)); Below a critical temperature (determined by the specific heat peak), the  $Z_8$  anisotropy

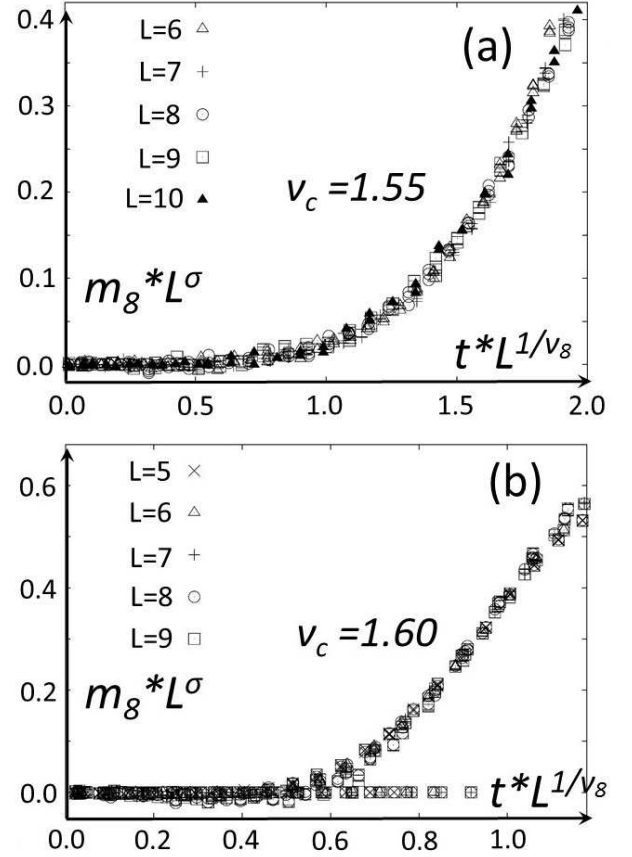


FIG. 12: Single-parameter scalings for the  $Z_8$  SB order parameter at  $D = 0$  with different parameter points; (a)  $(J, G) = (0.11, -0.99)$  (b)  $(J, G) = (0.31, -0.95)$ .

always becomes prominent in the O(3) sphere even for the smallest simulated system size ( $L = 6$ ).

On the one hand, we also observe an unexpected O(3) to  $Z_8$  crossover region below the bicritical point at  $G < 0$  and  $D = 0$  (Fig. 10(a)). Fig 11 shows a set of temperature dependences of the O(3) order parameter  $m$  and  $Z_8$  order parameters  $m_{c,\mu}$  ( $\mu = 1, 2, 3$ ) calculated for different system sizes and at two different parameter points in the  $Z_8$  SB phase region at  $G < 0$  and  $D = 0$ ;

$$m \equiv \sqrt{m_1^2 + m_2^2 + m_3^2}$$

$$m_{c,\mu} \equiv \epsilon_{\mu\nu\rho} \frac{(m_\nu + im_\rho)^4 + (m_\nu - im_\rho)^4}{2m^3}.$$

Three  $Z_8$  SB order parameters ( $\mu = 1, 2, 3$ ) show the same temperature dependence. Fig. 12 shows one-parameter scaling forms for the  $Z_8$  SB order parameters;  $m_{c,\mu} = L^{-\sigma} g_c(tL^{1/\nu_c})$ . To obtain them, we fixed  $\nu$  and  $\beta$  to be those of 3D cubic fixed point ( $\nu = 0.704$  and  $\beta = 0.362$ )<sup>38</sup>, while we fine-tuned  $T_c$  and  $\nu_c$  to fit data points for  $m$  and  $m_{c,\mu}$  ( $\mu = 1, 2, 3$ ) into  $g(x)$  (not shown) and  $g_c(x)$  (Fig. 12) respectively. The optimal  $\nu_c$  thus determined is  $1.55 \pm 0.05$  at the two different parameter points.

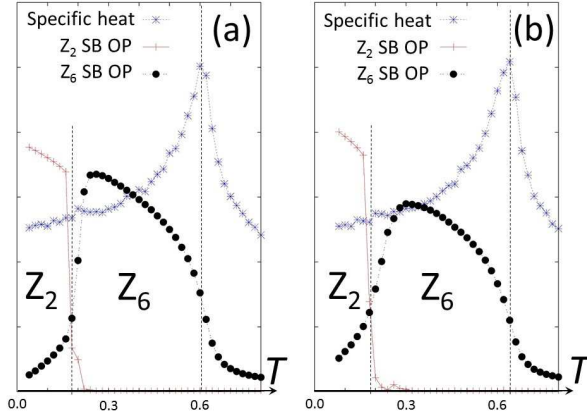


FIG. 13: Temperature dependencies of  $Z_2$  SB order parameter (red cross points), XY order parameter (black filled circle points) and specific heat (blue double cross points) around the phase boundary between  $Z_2$  SB phase and  $Z_6$  SB phase; (a)  $(J, D, G) = (0.05, -0.36, -0.93)$  (b)  $(J, D, G) = (-0.05, 0.25, -0.97)$

The  $O(3)$  to  $Z_8$  crossover at  $G < 0$  and  $D = 0$  is apparently counterintuitive from the viewpoint of the previous studies on the  $O(n)$  vector model with the cubic anisotropy.<sup>38</sup> A simple explanation for this is that the cubic anisotropy at the microscopic Hamiltonian level is much smaller than  $T_c$  and because the largest simulated system size ( $L = 10$ ) is still too small that renormalized (thus enhanced) cubic term is tiny compared to  $T_c$ . In fact, the cubic term vanishes completely at the unfrustrated  $SU(2)$  point;  $(J, D, G) = (0, 0, -1)$ , while  $T_c$  takes the largest value at this  $SU(2)$  point (see  $\theta = \pi$  in Fig. 10(a)). Besides, a positive scaling dimension of the cubic term around the 3D Heisenberg fixed point was suggested to be very small.<sup>38</sup>

### Appendix C: MC evidence for the first order phase transition between $Z_2$ and $Z_6$ SB phases

Fig. 13 shows a set of temperature dependence of the  $Z_2$  SB order parameter and that of XY order parameter

(order parameter for the  $Z_6$  SB phase) around finite- $T$  phase boundaries between  $Z_2$  phase and  $Z_6$  phase. The results show discontinuous changes of these two order parameters at the phase boundaries, indicating that the transition is of the first order.

To obtain them, we defined these two order parameters as follows. According to the group theory analysis<sup>5</sup>,  $\mathbf{H}(\mathbf{k} = 0)$  has two 1D irreducible representations which have the same index table and which correspond to the lowest eigenstate of  $\mathbf{H}(\mathbf{k} = 0)$  in the  $Z_2$  SB phase region. Let us call their bases as  $|\phi_3^{(1)}\rangle$  and  $|\phi_3^{(2)}\rangle$  respectively. Note also that  $\mathbf{H}(\mathbf{k} = 0)$  has three 2D irreducible representations which have the same index table and which correspond to the doubly degenerate lowest eigenstates of  $\mathbf{H}(\mathbf{k} = 0)$  in the  $Z_6$  SB phase region. Call respective three sets of doubly degenerate bases as  $|\phi_1^{(l)}\rangle$  and  $|\phi_2^{(l)}\rangle$  ( $l = 1, 2, 3$ ).

The order parameter for the  $Z_2$  SB phase is given by a linear combination of the following two quantities;

$$t_m = \sum_{j,\alpha} S_{j,\alpha} \langle j, \alpha | \phi_3^{(m)} \rangle$$

with  $m = 1, 2$  and  $j$  sublattice index,  $\alpha$  spin index. In Fig. 13, the temperature dependence of either  $t_1$  or  $t_2$  is shown as the  $Z_2$  SB order parameter. The XY order parameter for the  $Z_6$  SB phase is given by a combination of the following three quantities;

$$m^{(l)} \equiv \sqrt{(m_1^{(l)})^2 + (m_2^{(l)})^2}$$

with  $l = 1, 2, 3$  and

$$m_m^{(l)} \equiv \sum_{j,\alpha} S_{j,\alpha} \langle j, \alpha | \phi_m^{(l)} \rangle$$

with  $m = 1, 2$ . In Fig. 13, the temperature dependence of one of  $m^{(1)}$ ,  $m^{(2)}$  and  $m^{(3)}$  is shown as the XY order parameter for the  $Z_6$  SB phase.

\* Electronic address: rshindou@pku.edu.cn

<sup>1</sup> K. I. Kugel and D. I. Khomskii, Sov. Phys. Usp. **25**, 231 (1982).

<sup>2</sup> B. J. Kim, H. Ohsumi, T. Komesu, S. Sakai, T. Morita, H. Takagi, and T. Arima, Science, **323**, 1329 (2009).

<sup>3</sup> G. Jackeli and G. Khaliullin, Phys. Rev. Lett. **102**, 017205 (2009).

<sup>4</sup> J. Chaloupka, G. Jackeli and G. Khaliullin, Phys. Rev. Lett. **105**, 027204 (2010).

<sup>5</sup> G. Chen and L. Balents, Phys. Rev. B, **78**, 094493 (2008)

<sup>6</sup> A. Kitaev, Ann. Phys. (N. Y.) **321**, 2 (2006).

<sup>7</sup> Y. Singh and P. Gegenwart, Phys. Rev. B. **82**, 064412 (2010)

<sup>8</sup> X. Liu, T. Berlijn, W. G. Yin, W. Ku, A. M. Tsevelik, Y. J. Kim, H. Gretarsson, Y. Singh, and P. Gegenwart, and J. P. Hill, Phys. Rev. B **83**, 220403 (R) (2011)

<sup>9</sup> S. K. Choi, R. Coldea, A. N. Kolmogorov, T. Lancaster, I. I. Mazin, S. J. Blundell, P. G. Radaelli, Y. Singh, P. Gegenwart, K. R. Choi, S. W. Cheong, P. J. Baker, C. Stock, and J. Taylor, Phys. Rev. Lett. **108**, 127204 (2012).

- <sup>10</sup> F. Ye, S. Chi, H. Cao, B. C. Chakoumakos, J. A. Fernandez-Baca, R. Custelcean, T. F. Qi, O.B. Korneta, and G. Cao, Phys. Rev. B **85** 180403 (R) (2012).
- <sup>11</sup> M. J. O'Malley, H. Verweij and P. M. Woodward, J. Solid State Chem. **181**, 1803 (2008).
- <sup>12</sup> Y. Singh, S. Manni, J. Reuther, T. Berlijn, R. Thomale, W. Ku, S. Trebst, and P. Gegenwart, Phys. Rev. Lett. **108** 127203 (2012).
- <sup>13</sup> T. Takayama, A. Kato, R. Dinnebier, J. Nuss and H. Takagi, arXiv:1403.3296 (2014).
- <sup>14</sup> A. Biffin, R. D. Johnson, Sungkyun Choi, F. Freund, S. Manni, A. Bombardi, P. Manuel, P. Gegenwart, and R. Coldea, arXiv:1408.0246 (2014).
- <sup>15</sup> K. A. Modic, T. E. Smidt, I. Kimchi, N. P. ZBreznay, A. Biffin, S. Choi, R. D. Johnson, R. Coldea, P. Watkins-Curry, G. T. McCandless, J. Y. Chan, F. Gandara, Z. Islam, A. Vishwanath, A. Shekhter, R. D. McDonald, and J. G. Analytis, Nature Comm, **5**, 4203 (2014).
- <sup>16</sup> A. Biffin, R. D. Johnson, I. Kimchi, R. Morris, A. Bombardi, J. G. Analytis, A. Vishwanath and R. Coldea, arXiv:1407.3954 (2014).
- <sup>17</sup> Y. Okamoto, M. Nohara, H. Aruga-Katori, and H. Takagi, Phys. Rev. Lett. **99** 137207 (2007).
- <sup>18</sup> Y. Singh and P. Gegenwart, Phys. Rev. B, **88** 220413(R) (2013).
- <sup>19</sup> R. Dally T. Hogan, A. Amato, H. Luetkens, C Baines, J. Rodriguez-Rivera, M. J. Graf, and S. D. Wilson, Phys. Rev. Lett. **113**, 247601 (2014).
- <sup>20</sup> A.C. Shockley, F. Bert, J-C. Orain, Y. Okamoto, and P. Mendels Phys. Rev. Lett. **115**, 047201 (2015).
- <sup>21</sup> M. J. Lawler, H. Y. Kee, Y. B. Kim, and A. Vishwanath, Phys. Rev. Lett. **100**, 227201 (2008).
- <sup>22</sup> Y. Zhou, P. A. Lee, T. K. Ng, and F. C. Zhang, Phys. Rev. Lett. **101**, 197201 (2008).
- <sup>23</sup> M. J. Lawler, A. Paramakanti, Y. B. Kim, and L. Balents, Phys. Rev. Lett. **101**, 197202 (2008).
- <sup>24</sup> M. E. Zhitomirsky, Phys. Rev. B **78**, 094423 (2008).
- <sup>25</sup> E. J. Bergholtz, A. Läuchli and R. Moessner, Phys. Rev. Lett. **105**, 237202 (2010).
- <sup>26</sup> I. Kimchi and A. Vishwanath, Phys. Rev. B **89** 014414 (2014).
- <sup>27</sup> M. Norman and T. Micklitz, Phys. Rev. B **81**, 024428 (2010).
- <sup>28</sup> T. Micklitz and M. Norman, Phys. Rev. B **81** 174417 (2010).
- <sup>29</sup> M. Creutz, Phys. Rev. D **36**, 515 (1987).
- <sup>30</sup> K. Kanki, D. Loison, and K. D. Schotte, Eur. Phys. J. B **44**, 309 (2005).
- <sup>31</sup> J. M. Luttinger and L. Tisza, Phys. Rev. **70**, 954 (1946).
- <sup>32</sup> J. M. Luttinger Phys. Rev. **81**, 1015 (1951).
- <sup>33</sup> D. Blankschtein, M. Ma, A.N. Berker, G.S. Grest, and C.M. Soukoulis, Phys. Rev. B **29**, 5250 (1984).
- <sup>34</sup> M. Oshikawa, Phys. Rev. B **61**, 3430 (2000)
- <sup>35</sup> J. Lou, A. W. Sandvik, and L. Balents, Phys. Rev. Lett. **99**, 207203 (2007).
- <sup>36</sup> T. Okubo, K. Oshikawa, H. Watanabe, N. Kawashima, Phys. Rev. B **91**, 174417 (2015).
- <sup>37</sup> M. Campostrini, M. Hasenbusch, A. Pelissetto, P. Rossi, and E. Vicari, Phys. Rev. B **63**, 214503 (2001).
- <sup>38</sup> A. Pelissetto and E. Vicari, Physics Reports **368** (6), 549-727 (2002).
- <sup>39</sup> C. C. Price and N. B. Perkins, Phys. Rev. Lett. **109** 187201 (2012).
- <sup>40</sup> C. C. Price and N. B. Perkins, Phys. Rev. B **88** 024410 (2013).
- <sup>41</sup> T. Holstein and H. Primakoff, Phys. Rev. **58**, 098 (1940).
- <sup>42</sup> L. D. C. Jaubert, O. Benton, J. G. Rau, J. Oitmaa, R. R. P. Singh, N. Shannon, and M. J. P. Gingras, arXiv:1505.05499v1